

EXECUTIVE SUMMARY

Numerical simulations of the deformations and breakup of drops have been done. A finite difference/front tracking numerical technique is used to solve the unsteady axisymmetric Navier-Stokes equations for both the drops and the ambient fluid. Inertial, viscous, and surface tension effects are all accounted for. The simulations help determine where in parameter space the various breakup modes take place, how long breakup takes, and what the resulting drop size distribution is. The goal of the investigation is to provide results that extend and complement experimental investigations, and lead to better engineering models of drops in sprays.

In order to simulate the drop breakup at small density ratios (relevant to fuel sprays near critical conditions), two cases are examined in detail: a density ratio close to unity ($\rho_d/\rho_o = 1.15$) and a density ratio of 10. In both cases, the drops are accelerated impulsively. The results with the lower density ratio can be re-scaled to predict the drop behaviors at other density ratios close to one, by applying the Boussinesq approximation. In addition to full simulations where the Navier-Stokes equations are solved, a few inviscid simulations have also been done to identify the physical mechanism causing drop breakup.

Four non-dimensional numbers govern the breakup of drops. In addition to the density and the viscosity ratio, the ratio of inertia to surface tension is described by the Weber number, whereas the ratio of inertia to viscous force is represented by the Reynolds number. Sometimes, these two numbers are combined to yield the Ohnesorge number ($Oh=\sqrt{We}/Re$), which is the ratio of the viscous force to the surface tension. The simulations have resulted in a fairly complete picture of the evolution at small density ratios. When the effect of viscosity is not significant ($Oh < 0.1$), the Weber number has the dominant effects: For small Weber numbers, the drops display oscillatory deformation, independent of the density ratio, since the surface tension limits the deformation. As the Weber number is increased, the drops deform into a disk-like shape first, due to high pressure at the fore and aft stagnation points and low pressure around the equator. As the deformation progresses, the bulk of the drop fluid ends up in a thick rim connected by a thin film. At moderate Weber numbers, the rim eventually moves faster than the film and a backward-facing bag is formed. This backward-facing bag mode is only observed for the density ratio 10 simulations. In the lower density ratio, 1.15, the difference between the drop and the fluid inertia vanishes quickly and the surface tension pulls the drops back into

REPORT DOCUMENTATION PAGE

Public reporting burden for this collection of information is estimated to average 1 hour per response, including the time data needed, and completing and reviewing this collection of information. Send comments regarding this burden estimate to Washington Headquarters Services, Directorate for Information Operations and Reports, 1215 Jefferson Management and Budget, Paperwork Reduction Project (0704-0188), Washington, DC 20503.

000			18	D maintaining the ions for reducing ce of
			AFRL-SR-BL-TR-00-	
			0782	
1. AGENCY USE ONLY (Leave blank)		2. REPORT DATE, 3/31/00	3. REPC Final Technical Report 7/1/99-12/31/99	
4. TITLE AND SUBTITLE (U) Computational Investigation of Atomization			5. FUNDING NUMBERS PE - 61102F PR - 2308 SA - BX G - F49620-99-1-0314	
6. AUTHOR(S) Gretar Tryggvason				
7. PERFORMING ORGANIZATION NAME(S) AND ADDRESS(ES) University of Michigan Dept. of Mechanical Engineering 2031 Lay Automotive Lab. Ann Arbor, MI 48109-2121			8. PERFORMING ORGANIZATION REPORT NUMBER	
9. SPONSORING / MONITORING AGENCY NAME(S) AND ADDRESS(ES) AFOSR/NA 801 North Randolph Street Room 732 Arlington, VA 22203-1977			10. SPONSORING / MONITORING AGENCY REPORT NUMBER	
11. SUPPLEMENTARY NOTES				
12a. DISTRIBUTION / AVAILABILITY STATEMENT Approved for public release; distribution is unlimited			12b. DISTRIBUTION CODE	
13. ABSTRACT (Maximum 200 Words) The secondary breakup of liquid fuel drops was studied by numerical simulations. The Navier-Stokes equations were solved by a finite difference/front tracking technique that included inertia, viscous forces, and surface tension at the deformable boundary between the fuel and the air. The breakup of drops accelerated impulsively was studied by axisymmetric simulations for two different density ratios (1.15 and 10). The low density ratio results can be used for other density ratios by simple rescaling of time. It was shown that the drops break up in different modes, depending on the relative strength of surface tension versus inertia. The modes are similar to those found experimentally for drops in air at atmospheric pressure and breakup maps constructed from the computational results show similar transitions. There are, however, some differences. Bag breakup is, for example, not found for impulsively accelerated drops in the low density ratio limit. Computations of the breakup of cold drops in hot ambient show a rapid increase in heat transfer, and the drops often reach the ambient temperature before breakup is completed.				
14. SUBJECT TERMS Atomization, Spray, Secondary breakup of drops			15. NUMBER OF PAGES 45	
			16. PRICE CODE	
17. SECURITY CLASSIFICATION OF REPORT Unclassified		18. SECURITY CLASSIFICATION OF THIS PAGE Unclassified	19. SECURITY CLASSIFICATION OF ABSTRACT Unclassified	20. LIMITATION OF ABSTRACT UL

a spherical shape. Increasing the Weber number further results in a different mode of breakup, where the fluid initially still ends up in the rim of the drop, but the initial momentum is now sufficiently large so the ambient fluid moves the film faster than the rim, forming a forward-facing bag. Comparisons with inviscid flow simulations show that the formation of a forward-facing bag is essentially an inviscid phenomenon. At very high Weber numbers, small drops are pulled from the rim at density ratio of 10, while interface roll-ups are observed at the lower density ratio, 1.15. The Reynolds number has a secondary effect: As the Reynolds number decreases, the critical Weber numbers for the transitions between breakup modes move to higher values. Increasing the viscosity ratio results in reduced deformation. The simulations have been used to generate “break-up” maps and it is found that the general character of those maps agrees with what has been found experimentally for larger density ratios.

In order to examine the effect of drop deformation and breakup on heat transfer, a preliminary study has been done for drops with initial temperature below that of the ambient fluid. Only drops with a small density ratio, 1.15, accelerated by a constant body force have been examined. The observed breakup modes are similar to those for impulsively accelerated drops. The only difference is that now the Eötvös number replaces the role of the Weber number: As Eo increases, different breakup modes—steady deformation into an oblate ellipsoidal shape; formation of a backward-facing bag; transient deformation; formation of a forward-facing bag—are seen. The rate of deformation also increases, as Eo becomes higher. When either a backward-facing bag or a forward-facing bag is formed, a rapid increase of the drop surface area occurs. The results show that the heat transfer between the drop and the ambient fluid is significantly influenced by the deformation.

Personnel Supported:

Grétar Tryggvason, Professor
Jaehoon Han, Research Fellow

Publications

J. Han and G. Tryggvason. Secondary Breakup of Axisymmetric Liquid Drops—Part II, Impulsive Acceleration. Submitted to *Phys. Fluids*.

J. Han and G. Tryggvason. Secondary Breakup of Liquid Drops in Axisymmetric Geometry—Part I. Acceleration by a Constant Body Force. *Phys. Fluids* 11 (1999), 3650-3667.

J. Han and G. Tryggvason. Secondary Breakup of drops. Proceedings of the 1999 ASME Fluids Engineering Division Summer Meeting, San Francisco, CA July 18-22, 1999.

J. Han and G. Tryggvason. Energy Transfer in the Secondary Breakup of Liquid Drops. Proceedings of the 2000 ASME Fluids Engineering Division Summer Meeting, Boston, MA June 11-16, 2000.

Presentations

G. Tryggvason. Invited Seminar at Rutgers University, 2/12/99.

G. Tryggvason. Lectures as part of a "Short Course on Modeling and Computation of Multiphase Flow, Part IIB: Multiphase flow CFD", March 8-12, 1999. Zurich, Switzerland.

G. Tryggvason. Direct Numerical Simulations of Multiphase Flow. American Physical Society Centennial Meeting, Atlanta, GA. March 20-26, 1999. Invited talk in a special session organized by the computational physics division of APS at the APS Centennial meeting in Atlanta.

G. Tryggvason. Direct Numerical Simulations of Dispersed Flow. 9th Workshop on Two-Phase Flow Predictions, Merseburg, Germany, April 13-16, 1999.

G. Tryggvason. Co-organizer and co-principal lectures in a short course: Suivis d'interfaces, INRIA Rocquencourt, France, May 3-6, 1999.

G. Tryggvason. Invited presentation: Direct Numerical Simulations of Atomization. 12th Annual Conference on Liquid Atomization and Spray Systems, Indianapolis, IN, May 16-19, 1999.

G. Tryggvason. Direct Simulations of Disperse Flows. ICIAM 99, Edinburg, Scotland, July 5-9, 1999.

G. Tryggvason. Direct Simulations of Multiphase Flows. Invited talk. Interfaces for the 21 century. Monterey, CA. August 16-18, 1999.

J. Han and G. Tryggvason. Heat Transfer in the Secondary Breakup of Liquid Drops. 52nd Meeting of the American Physical Society, Division of Fluid Dynamics, New Orleans, LA, Nov. 21-23, 1999.

G. Tryggvason. Invited Seminar at UCSD, 1/14/00.

G. Tryggvason. Invited Seminar at John Hopkins University, 2/17/00.

G. Tryggvason. Direct Simulations of Multiphase Flows. Invited talk. Institute for Multiphase Science and Technology (IMuST) Annual Meeting. Santa Barbara, CA. March 12-14, 2000.

G. Tryggvason. Lectures as part of a "Short Course on Modeling and Computation of Multiphase Flow, Part IIB: Multiphase flow CFD", Zurich, Switzerland. March 20-24, 2000.

Contents

I	Background	1
II	Formulation and numerical method	3
A	Navier-Stokes equations	3
B	Inviscid flow	5
III	Secondary breakup of drops due to impulsive acceleration	6
A	Effect of We at a fixed Re	7
1	Evolution of drops with $\rho_d/\rho_o = 10$	7
2	Evolution of drops with $\rho_d/\rho_o = 1.15$	9
B	Effect of Re	10
C	Effect of Re_d	11
D	Deformation and breakup regime map	11
IV	Simulations of heat transfer during breakup	12
V	Figures	16
VI	References	37

I. BACKGROUND

In spray combustion, secondary atomization of liquid droplets plays an important role in the increase of surface area and the enhancement of heat and mass transfer between the fuel and the ambient gas. In a separate report provided previously, we have discussed in detail the secondary breakup of liquid drops that are accelerated by a constant body force. The Eötös number, which is the ratio of the body force to the surface tension, was found to be the main controlling parameter. The fluid viscosities and the density ratio had secondary effects. Here, we focus on another type of disturbance causing drop breakup: impulsive acceleration of the droplet. This corresponds to an experimental situation where a liquid droplet is accelerated by a shock wave. This type of disturbance was employed in many experimental studies of secondary breakup. Earlier studies include Lane¹, Hinze², Hanson *et al.*³, Ranger and Nicholls⁴, and Gel'fand *et al.*⁵. For more recent studies of liquid atomization, see Krzeczkowski⁶, Borisov *et al.*⁷, Reitz and Bracco⁸, Pilch and Erdman⁹, Wierzbka¹⁰, Hsiang and Faeth^{11–13}, and Joseph *et al.*¹⁴.

Experimental results are usually presented in terms of four non-dimensional numbers: the Weber number We , the Reynolds number Re , the density ratio and the viscosity ratio. The Reynolds number is sometimes replaced by the Ohnesorge number. These numbers are defined later in the paper. The experimental data shows that the breakup of drops in gas flows can generally be categorized into six different modes¹⁵:

1. Vibrational breakup mode where the original drop disintegrates into two or four equal-sized smaller drops.
2. Bag breakup mode where the original drop deforms into a torus-shaped rim spanned by a thin fluid film that ruptures into tiny droplets, followed by the disintegration of the rim into larger droplets. Sometimes, a tiny streamer is also formed inside the bag, called the parachute or the umbrella breakup mode.
3. Transitional mode where irregular or chaotic fragmentation takes place. In this mode, the drop breaks up due to both the formation of a bag and the stripping of fluid from the drop

surface in the form of stretched fluid filaments.

4. Shear breakup mode where continuous stripping of fluid from the drop surface occurs.
5. Explosive breakup mode where strong surface waves disintegrate the drop in a violent manner.

In modes 2–4, the breakup process is initiated by the axisymmetric flattening of the drop into an ellipsoid or disk shape. For modes 1 and 5, the formation of a disk is not seen and there are good reasons to believe that the breakup is fully three-dimensional from the start. This categorization and terminology are somewhat arbitrary and different variations have been suggested by different researchers. For example, mode 2 has also been called “bag-and-stamen breakup” by Pilch and Erdman⁹ and “bag-jet mechanism” by Krzeczkowski⁶.

The transitions between the breakup modes described above take place at critical Weber numbers that generally depend only weakly on the Ohnesorge number. For low viscosity drops, the critical Weber numbers are approximately 10, 20, 30, 60, and 1000, respectively for the transitions from one mode to the next one. It is also found that the critical Weber numbers increase as the Ohnesorge number increases. Note that the first four breakup modes are realized for a very narrow range of Weber numbers. Wierzbba¹⁰ found that in the range of $11 \leq We \leq 14$, the drop deformation and the breakup are very sensitive to small fluctuations of the experimental conditions and he could further refine the observed breakup into five sub-categories. There are large variations in the critical Weber numbers in the available experimental data due to different test conditions. Thus the numbers presented above should be considered only as a rough guide.

Most previous studies have been done for liquid–gas systems at atmospheric pressure and temperature. The behavior of liquid droplets at smaller density ratios (characteristic of high pressure combustion systems) is not well-understood yet. In this study, computational results are presented for impulsively started drops in which the motion and deformation of the drop is caused by the initial momentum due to a step change in the relative velocity. Numerical simulations have been done for two density ratios, 1.15 and 10. These values are in the range of typical density ratios encountered in practical spray combustion systems (density ratios of $O(10)$ for diesel engines¹⁶

and $O(1)$ for rocket motors are common). Simulations in the Boussinesq limit using the smaller density ratio, 1.15, can be extended to predict the drop behavior at other density ratios close to 1. The effects of the individual governing parameters are examined and the physical mechanisms associated with different breakup modes are discussed.

II. FORMULATION AND NUMERICAL METHOD

A. Navier-Stokes equations

The physical problem and the computational domain are sketched in Figure 1. The domain is axisymmetric and the left boundary is the axis of symmetry. We solve for the motion everywhere, both inside and outside the drop. The Navier-Stokes equations are valid for both fluids, and a single set of equations can be written for the whole domain as long as the jump in density and viscosity is correctly accounted for and surface tension is included.

The Navier-Stokes equations in conservative form are:

$$\frac{\partial \rho \mathbf{u}}{\partial t} + \nabla \cdot (\rho \mathbf{u} \mathbf{u}) = -\nabla p + \nabla \cdot \mu (\nabla \mathbf{u} + \nabla \mathbf{u}^T) + \sigma \int_S \delta(\mathbf{x} - \mathbf{x}_f) (\mathbf{n} \times \nabla) \times \mathbf{n} dS. \quad (1)$$

Here, \mathbf{u} is the velocity, p is the pressure, and ρ and μ are the discontinuous density and viscosity fields, respectively. σ is the surface tension and δ is a three-dimensional delta function. Here, the surface tension is treated as a singular body force and its contribution is limited to the interface itself. The integral over the surface of the drop, S , results in a force distribution that is smooth and continuous along the drop surface.

The above equations are supplemented by the incompressibility condition:

$$\nabla \cdot \mathbf{u} = 0 \quad (2)$$

and equations of state for the physical properties:

$$\frac{D\rho}{Dt} = 0; \quad \frac{D\mu}{Dt} = 0 \quad (3)$$

where D/Dt is the total derivative. These two equations simply state that the physical properties within each fluid remain constant in the case of immiscible fluids.

Dimensional analysis shows that a set of four independent dimensionless parameters can be constructed for the dynamics of drop deformation and breakup. When the drop is subject to an impulsive acceleration, it is convenient to choose the Weber number, We , the Reynolds number based on the ambient fluid properties, Re , density ratio, and the Reynolds number based on the drop fluid properties. These are defined by:

$$We = \frac{\rho_o U^2 D}{\sigma}; Re = \frac{\rho_o U D}{\mu_o}; \frac{\rho_d}{\rho_o}; Re_d = \frac{\rho_d U D}{\mu_d}. \quad (4)$$

Sometimes, the drop Reynolds number is replaced by viscosity ratio, μ_d/μ_o . Here, D is the initial diameter of the drop and U is the initial relative velocity between the drop and the ambient fluid. The subscripts, d and o , denote the properties of the drop and the ambient fluid, respectively. Another parameter often used in the literature is the Ohnesorge number, $Oh = \mu/\sqrt{\rho D \sigma} = \sqrt{We}/Re$, which is the ratio of the viscous shear to the surface tension.

The momentum equations and the continuity equation are discretized using an explicit second-order predictor-corrector time-integration method combined with a second-order centered difference method for the spatial derivatives. The discretized equations are solved on a fixed, staggered grid. In order to improve the accuracy of the computation in some specific regions, non-uniform grid spacing is used. The full-slip boundary condition is applied to all four boundaries unless specified otherwise. For simulations with $\rho_d/\rho_o = 1.15$, a fixed computational domain is used whereas for the $\rho_d/\rho_o = 10$ simulations, a reference frame moving with the centroid of the drop is used. This enables us to keep the computation at a reasonable cost, while maintaining the necessary resolution around the moving drop. In order to accurately simulate a highly-deformed interface during breakup, a front-tracking method is employed, where the interface is represented by marker points that are moved by interpolating their velocities from the stationary grid. These points are connected to form a “front” which is used to construct the property fields at each time step. This front is also used to calculate the surface tension. For a more detailed description of the front tracking method, see Tryggvason, Bunner, Ebrat, and Tauber¹⁸. The majority of the simulations presented here were carried out on HP 9000 workstations. A typical run generally required between 4000 and 120000 time-steps and took 12–240 hours, depending on the parameters of the

problem.

B. Inviscid flow

To address to what extend the drop evolution can be described by an inviscid model, a few simulations were done using a vortex method. The interface separating the drop and the ambient fluid is a vortex sheet and an evolution equation for the vortex sheet strength $\gamma = (\mathbf{u}_d - \mathbf{u}_o) \cdot \mathbf{s}$ can be derived by subtracting the tangential components of the Euler equations on either side of the interface. The resulting equation is (see, for example, Tryggvason, 1988):

$$\frac{D\gamma}{Dt} + \gamma \frac{\partial \mathbf{U}}{\partial s} \cdot \mathbf{s} = 2A \left(\frac{D\mathbf{U}}{Dt} \cdot \mathbf{s} + \frac{1}{8} \frac{\partial \gamma^2}{\partial s} \right) - \frac{\sigma}{\rho_d + \rho_o} \frac{\partial \kappa}{\partial s}. \quad (5)$$

Here, $A = (\rho_d - \rho_o)/(\rho_d + \rho_o)$ is the Atwood number, $\mathbf{U} = (\mathbf{u}_d + \mathbf{u}_o)/2$ is the average of the velocities on either side of the vortex sheet, and κ is the mean curvature. Given the vortex sheet strength γ , the velocity is found by the Biot-Savart integral. For computational purpose, the axisymmetric vortex sheet is discretized by a finite number of vortex rings. The azimuthal integration can be done analytically and the integral is therefore replaced by a summation over the discrete vortex rings. The radial and axial velocities at a point on ring j are given by

$$u_j = \frac{1}{\pi} \sum_{l=1}^N \frac{\Gamma_l r_l k_{lj}(z_j - z_l)}{(4r_j r_l)^{3/2}} \left[\left(\frac{k_{lj}^2 - 2}{1 - k_{lj}^2} \right) E(k_{lj}) + 2K(k_{lj}) \right] \quad (6)$$

$$v_j = \frac{1}{\pi} \sum_{l=1}^N \frac{\Gamma_l r_l k_{lj}}{(4r_j r_l)^{3/2}} \left[\left(\frac{(r_l + r_j)k_{lj}^2 - 2r_l}{1 - k_{lj}^2} \right) E(k_{lj}) + 2r_l K(k_{lj}) \right]. \quad (7)$$

Here $K(k)$ is the Complete Elliptic integral of the first kind, and $E(k)$ is the Complete Elliptic integral of the second kind and

$$k_{lj} = \frac{2\sqrt{r_l r_j}}{\sqrt{(r_l + r_j)^2 + (z_j - z_l)^2}}. \quad (8)$$

The Elliptic integrals can be computed efficiently by a polynomial approximation¹⁹. When the axisymmetric vortex sheet is replaced by discrete vortex rings, the rings must be given a finite core size to avoid infinite self-induced velocity. This can be accomplished simply by replacing k_{lj} by

$$\tilde{k}_{lj} = \frac{2\sqrt{r_l r_j}}{\sqrt{(r_l + r_j)^2 + (z_j - z_l)^2 + \delta^2}} \quad (9)$$

where δ is a small regularization parameter that determines the size of a “vortex blob”. In the limit of $N \rightarrow \infty$ and $\delta \rightarrow 0$ the solution will be independent of the exact value of δ (except at isolated points where roll-up takes place).

The evolution equation for the circulation of each vortex ring can be obtained by integrating Equation (5) over a small material segment:

$$\frac{D\Gamma}{Dt} = 2A \int_{s(\alpha^-)}^{s(\alpha^+)} \left[\frac{DU}{Dt} \cdot \mathbf{s} + \frac{1}{8} \frac{\partial \gamma^2}{\partial s} \right] ds - \frac{\sigma}{\rho_d + \rho_o} [\kappa(\alpha^+) - \kappa(\alpha^-)] \quad (10)$$

where α^+ and α^- are the two end points of the segment. Equation (10), along with the equation $D\mathbf{x}/Dt = \mathbf{U}$, where $\mathbf{x} = (r, z)$ is the position vector for each vortex ring, can be integrated using a time-integration method such as the fourth-order Runge-Kutta method, once the initial vorticity distribution and the geometry are given. The DU/Dt term is found in an iterative manner: First the interface is advanced and the circulations are updated using DU/Dt from last time-step as an approximation. Then the velocities at the new position are found using the approximate value of the circulations. The velocities are then used to calculate DU/Dt at the original interface position and the process is repeated.

III. SECONDARY BREAKUP OF DROPS DUE TO IMPULSIVE ACCELERATION

Most of the simulations presented here are for $\rho_d/\rho_o = 10$. The effects of the Weber number, the Reynolds number, and the viscosity ratio are studied. In addition, a few simulations have been done for $\rho_d/\rho_o = 1.15$ to examine the effect of the density ratio. As discussed in part I, the Boussinesq approximation applies when the drop and the ambient fluid have similar densities. Thus a single simulation with one specific value of the density ratio close to 1 can be rescaled for a range of density ratios. When presenting the results, time is non-dimensionalized with the diameter and the initial relative velocity, $t^* = t/(D/U)$.

A. Effect of We at a fixed Re

1. Evolution of drops with $\rho_d/\rho_o = 10$

In Figure 2, the deformation and breakup of drops with $\rho_d/\rho_o = 10$ are shown for $Re = 242$ and $Re_d = 1935$. Results for $We = 3.74, 12.5, 18.7, 28.1, 37.4, 46.8, 56.1, 74.8, 93.5$ and ∞ are compared. For these parameters (excluding the $We = \infty$ case), the Ohnesorge numbers, Oh , are between 0.008–0.04. Experimental evidence suggest that when $Oh < 0.1$, the viscosity has only minor effects and that surface tension effects are dominant. The computations were done using a resolution of 256×512 grid points. The drop in (a) with $We = 3.74$ shows oscillatory deformation. The drops with $We = 12.5$ and 18.7 in (b) and (c) initially develop an indentation at the top and it continues to deepen. As the deformations increase the drag, the initial momentum of the drop fluid decreases. This reduces the aerodynamic pressure variations around the drop and the influence of the surface tension starts to increase. At later stages of the deformation, a backward-facing bag is formed. Eventually, the backward-facing bags in (b) and (c) stop growing and the drops restore their originally spherical shapes. The drop shown in (d) for $We = 28.1$ shows the formation of a backward-facing bag more clearly. The Weber numbers for the drops in (b)–(d) are in the range where a bag breakup mode is observed experimentally for higher density ratios. The results in (e)–(i), for even higher Weber numbers, show, on the other hand, the formation of a forward-facing bag. The drop with zero surface tension in (j) also displays a forward-facing bag. In this case small scale irregularities are observed both on the edge and on the top surface of the drop. This is due to the absence of the surface tension, which suppresses the formation of the small-scale structures caused by the interfacial shear.

The aspect ratio (the maximum width of the drop divided by its thickness at the centerline), centroid velocity, and surface area of some of the drops shown in Figure 2 are plotted versus non-dimensional time, t^* , in Figure 3. The aspect ratio plot displays an oscillation of the drop with the lowest We and monotonic decrease for the other drops. When the drops with $We = 12.5$ and 18.7 start to resume their initial shape, an abrupt increase in the aspect ratio is observed. The velocity

plot shows a monotonic decline for all We shown. The surface area plot shows that the rate of deformation increases with We .

In Figure 4 and 5, vorticity contours (left) and streamlines (right) at selected times are plotted along with the drop contour for the $We = 28.1$ and $We = 93.5$ drops shown in Figure 2(d) and (i) respectively. In both cases, the vorticity plots show that most of the vorticity is created at the outer edge of the drop, as expected. The streamline pattern for the $We = 28.1$ drop shows that the backward-facing bag is stretched upward when the wake downstream of the drop detaches from it. On the other hand, the closed streamlines around the $We = 93.5$ drop suggests that the drop moves as a vortex ring, forming a forward-facing bag.

Inviscid flow simulations using a vortex method are presented for $We = 93.5$ and $\rho_d/\rho_o = 10$ in Figure 6. The evolution of three inviscid drops with different blob sizes, $\delta = 0.0125, 0.01$, and 0.0075 , are shown in (a), (b), and (c), respectively. In addition, the viscous simulation for the same Weber number and the density ratio —already shown in Figure 2(i)— is illustrated again in (d) for comparison. In each column, the drop shapes are plotted every $t^* = 0.4835$. Note that δ was introduced in Equation (9) only to avoid singularity and that the choice of δ is somewhat arbitrary. The overall drop evolution is, however, not very sensitive to the exact value of δ : In all three cases, a thin film of drop liquid is pulled away from the shoulder of the main drop. Differences exist in the small scale structures such as the thickness of the film, which reduces faster for smaller δ . The viscous drop in (d) also displays an evolution similar to those of the inviscid drops.

The centroid velocities of the drops in Figure 6 (a)–(d) are compared in Figure 7. As the drops starts to move, the viscous simulation shows a faster decrease of the initial velocity, compared to the inviscid results. Later, the inviscid drops deform more and the trend is reversed. The degree of deformation of the inviscid drops also increases weakly as δ becomes smaller, so the velocity of an inviscid drop with a smaller δ decreases faster.

In spite of some differences, due to viscosity on the one hand and finite regularization on the other, the viscous drop and the inviscid ones display essentially the same behavior. Traditional “shear”² or “boundary-layer stripping”⁴ breakup theories are based on the assumption that viscous boundary layers develop on both side of the interface and viscous shear causes a portion of the drop

fluid to be stripped from the drop shoulder. The validity of this assumption has been questioned by Lee and Reitz²¹, whose experimental observations in the shear breakup regime were independent of the Reynolds number, suggesting weak influence from the viscous boundary layers. As an alternative, they proposed a “stretching–thinning” type breakup mechanism where the thin edge of the drop, flattened by the aerodynamic pressure, is deflected in the downstream direction by blowing of the ambient fluid. Our inviscid simulations show that the initial formation of the thin film from the drop shoulder is an inviscid phenomenon, supporting the “stretching–thinning type” mechanism.

2. Evolution of drops with $\rho_d/\rho_o = 1.15$

Figure 8 shows the deformation versus time of drops with a density ratio of 1.15 in the same way as in Figure 2. The Weber numbers are 2.73, 13.7, 27.4, 54.7, and ∞ , the Reynolds number is fixed at 331, and the drop-based Reynolds number is 381. The computations were done using a 128×256 grid. The low Weber number drop in (a) oscillates due to the high surface tension. As We is increased to 13.7, the drop starts to develop an indentation at the top as shown in (b) but as it falls, the momentum of the drop decreases and the surface tension causes it to oscillate. The drop shown in (c) for $We = 27.4$ also deforms into an indented ellipsoid initially. The indentation deepens progressively and later meets the bottom of the drop surface, forming a forward-facing bag as observed in the continuous acceleration case. However, since there is no force to maintain the motion, the drop eventually resumes its initial shape. The drop with $We = 54.7$ in (d), on the other hand, shows increased initial deformation which results in a bigger rim that is connected by a forward-facing bag. For zero surface tension, (e), the drop displays a roll-up of the interface. A similar roll-up has been observed in the constant acceleration cases for drops with no surface tension.

In Figure 9, the normalized aspect ratio, centroid velocity, and surface area are plotted versus t^* in (a)–(c), respectively, for the drops shown in Figure 8. The aspect ratio plot shows shape oscillation for the two lower values of We . For higher We , the aspect ratio decreases monotonically

to zero as the indentation deepens progressively. The velocity plot in (b) shows a rapid decline initially. Later, the velocity of the drops with $We = 2.73$ and 13.7 decreases but with fluctuations. The velocities of the drops with three higher Weber numbers decrease monotonically until it reaches a minimum and starts to increase again. The surface area plot in (c) show the effect of We on deformation: As We increases, the slope of the curve increases.

B. Effect of Re

In order to see the effect of the viscosity of the ambient fluid, simulations with four different Reynolds numbers, $Re = 387, 242, 121, 60.5$ (from left to right) are compared in Figure 10. In the top row (a), $We = 18.7$, $\rho_d/\rho_o = 10$, and $Re_d = 1935$. The overall evolution of the drops with two higher Reynolds numbers, $Re = 387$ and 242 , are very similar and the only difference is in the small scale structure of the drop contour. The results for the two lower Reynolds numbers, $Re = 121$ and 60.5 , however, display some differences: Increasing the ambient fluid viscosity (decreasing the Reynolds number) while the other parameters are fixed can lead to a transition from the backward-facing bag mode to the oscillatory deformation mode. Another comparison is made in (b) for $We = 74.8$, while other parameters remain the same as in (a). Here, a transition from the forward-facing bag mode to the backward-facing bag mode is observed as the Reynolds number is reduced from 121 to 60.5 .

Based on these observations, it is clear that progressively higher Weber numbers are necessary in order to observe the same mode of deformation, as the Reynolds number is decreased. The translation of the boundaries between different deformation modes—oscillation, backward-facing bag, and forward-facing bag—to higher We is clearly due to the increased viscous dissipation.

In Figure 11, the surface areas of the drops shown in Figure 10 are plotted versus the non-dimensional time, t^* . The comparison in (a) for drops with $We = 18.7$ indicates that the rate of increase of the surface area becomes higher as the Reynolds number increases, due to less viscous dissipation. The same trend is confirmed for $We = 74.8$ in (b).

C. Effect of Re_d

In Figure 12, the effect of drop viscosity is shown for drops with $\rho_d/\rho_o = 10$ and $Re = 242$. The figures in each frame denotes the dimensionless time when the drop is plotted. In the top row, four cases are compared for different drop viscosities (represented by the Reynolds number based on drop properties) at a fixed Weber number, $We = 28.1$. As the drop viscosity is increased from left to right by an order of 10^3 , the drop deformation is greatly reduced. The least viscous drop with $Re_d = 1935$ clearly shows the formation of a backward-facing bag, while the most viscous drop with $Re_d = 1.935$ remains in an oblate shape. In the middle row, a similar comparison is made for $We = 56.1$. Again, by increasing the drop viscosity, the drop deformation is reduced and the drop changes from a forward-facing bag to an oblate drop. The result for $We = 93.5$ drops shown in the bottom row also displays a similar trend.

D. Deformation and breakup regime map

In Figure 13(a), a breakup map is shown to summarize the deformation and breakup modes of drops with $\rho_d/\rho_o = 10$ and $Re_d = 1935$. The horizontal and vertical axes represent the Reynolds number and the Weber number based on the ambient fluid, respectively. The various breakup modes are denoted by different symbols. When the Weber number is low, surface tension prevents large deformation so the drop only oscillates. As the Weber number increases past a critical value (approximately 16) for high Re , a backward-facing bag starts to emerge. When the Weber number is higher than approximately 30, the drops break up in a backward-facing bag mode for low Reynolds numbers and in a forward-facing bag mode at high Reynolds numbers. The transitions from the backward-facing bag mode to the forward-facing bag mode occur at progressively lower Weber numbers as the Reynolds number increases. As the Weber number is raised to 100, approximately, all drops break up in the forward-facing bag mode for the Reynolds number range examined. Finally, when the surface tension vanishes ($We \rightarrow \infty$), the strong shear due to the outside flow peels off the drop interface and shear breakup is observed when the Reynolds number is greater than 100.

A similar breakup map is presented in Figure 13(b) for the drops with $\rho_d/\rho_o = 1.15$ and $Re_d = 1935$. Again, when the Weber number is low, the drops only oscillate due to large surface tension. As the Weber number is increased, the backward-facing bag mode displayed in (a) for $\rho_d/\rho_o = 10$ is no longer observed as the momentum difference between the drop and the ambient fluid is relatively smaller, in case of density ratio close to one. Instead, the drops in this Weber number range oscillate back into their initial spherical shapes. When the Weber number is greater than 100, the drop deforms into a forward-facing bag and the roll-up of the interface is observed. The effect of the Reynolds number is similar to what has been observed in (a): the boundaries between different deformation/breakup modes move to higher Weber numbers as the Reynolds number decreases.

IV. SIMULATIONS OF HEAT TRANSFER DURING BREAKUP

The ultimate reason for atomizing a fuel jet is to increase the evaporation rate of the fuel. Before evaporation, the fuel must heat up. As fuel drops break up, their surface area increases greatly and therefore the heat transfer to the drop. Simulating heat and mass transfer at intermediate Reynolds numbers, in addition to fluid flows is a very complicated problem. Under these circumstances, various transport mechanisms are involved and the accurate determination of the relative importance of each mechanism becomes a challenging task. Some simplifications are possible when the drop has transport properties considerably different from those of the surrounding fluid. For problems not involving a phase change, a comprehensive discussion of these approximations is given by Abramzon and Borde²². When both fluids have comparable transport properties, the problem becomes more complex and full numerical simulations are often employed. For example, studies of isolated, as well as interacting, vaporizing fuel droplets at intermediate Reynolds numbers are described by Chiang²³, Chiang and Sirignano²⁴ and Haywood *et al.*²⁵. In these studies, simulations are limited to cases with either small or moderate deformation.

Here, we examined the heat transfer during secondary breakup of drops with a small density ratio, $\rho_d/\rho_o = 1.15$. The drops are accelerated by a body force and have an initial temperature

lower than the surrounding fluid. Phase change and density variation with temperature are not considered. The temperature field at each time step is obtained by solving the unsteady energy equation. If heat generation due to viscous friction and radiation heat transfer is neglected, the energy equation is:

$$\frac{\partial \rho c_p T}{\partial t} + \nabla \cdot (\rho c_p T) = \nabla \cdot k \nabla T. \quad (11)$$

This equation is solved on a fixed grid by an explicit second order method in the same way as the momentum equation.

In Figure 14, the evolution of the drop interface is shown for different Eo . In all cases, $\rho_d/\rho_o = 1.15$. Values of Ohnesorge numbers, $Oh_o = 0.05$ and $Oh_d = 0.0466$, are chosen so that viscous effects are small compared to surface tension effects. The computations were done using a fixed coordinate system. When Eo is small, the drop is deformed into an oblate ellipsoidal shape and reaches a steady state as shown in (a) for $Eo = 2.4$. The drop shown in (b) for $Eo = 24$ initially develops an indentation at the top and later deforms into a disk-like shape. Then the thickness of the drop near the symmetry axis continues to decrease and most of the drop fluid moves outward toward the edge of the drop. Finally, the center portion of the front surface is pushed upward, forming a backward-facing bag. At this stage, most of the drop fluid is contained in the annular-shaped rim. As time progresses, the bag portion of the drop, which forms a thin membrane spanning the rim, expands both radially outward and vertically upward. Experimental evidence indicate that it will eventually break into smaller drops. In (c), where Eo is 48, the drop remains in a convex shape showing no sign of forming a bag while the shape oscillation continues during the entire time simulated. When Eo is 144 in (d), the indentation developed at the top of the drop deepens continuously until it reaches the bottom of the drop, creating a forward-facing bag. Eventually, the heavier edge falls faster than the thin bag.

Figure 15(a) shows vorticity contours (left) and streamlines (right) when the drop shown in Figure 14(b) develops a backward-facing bag. In the vorticity plot, most of the vorticity is created at the outer edge of the drop, as expected. The streamlines plotted with respect to a reference frame moving with the drop show that the backward-facing bag is stretched upward in the downstream

direction. The existence of the wake behind the drop is evident when the backward-facing bag is formed. Figures 15(b) illustrates vorticity contours (left) and streamlines (right) for the drop shown in Figure 14(d) when a forward-facing bag is formed. Again, much of the vorticity is created at the outer edge of the drop. However, the closed streamlines around the drop suggest that the drop is essentially a vortex ring. The size of the wake is smaller than in Figure 15(a).

In Figures 16, the surface area of the drop S (normalized by the initial value S_o) is plotted versus t^* for the drops shown in Figures 14 (a)–(d). Note that the surface area increases rapidly upon drop breakup. For example, the $Eo = 24$ drop, which deforms into a backward-facing bag, shows a nearly steady increase with some fluctuations. The slope of the graph is steeper when the drop is about to form the backward-facing bag but once the bag is formed and starts to grow in size, the slope is reduced. Meanwhile, the result for $Eo = 48$ shows an oscillatory behavior. The magnitude of the surface area fluctuations, however, does not grow. The graph for the drop with higher 144 illustrates a rapid initial increase as the drops deform into a forward-facing bag. It then decreases when the draining of the drop fluid from the symmetry axis is completed. When the heavy outer rim of the drop containing most of the drop fluid falls faster than the thin film near the symmetry axis, the total surface area of the drop starts to rapidly increase again due to the formation of a backward-facing bag.

The temperature field and the drop contour are plotted in Figure 17 for the drops shown in Figure 14 (a), (b), and (d). In all cases, the drops have identical thermal properties, $Pr = 1$, $k_d/k_o = 0.2$ and $c_{p,d}/c_{p,o} = 1$. The spherical drop is plotted at $t = 28$, the bag-breakup drop at $t = 28$, and the shear breakup drop at $t = 4$. The temperature field around the spherical drop shows that recirculation inside the drop leads to a ring of cold fluid inside the drop and a steep temperature gradient near the front of the drop. As the drop heats up, the ambient fluid cools down and a cold thermal wake extends downstream from the drop. The temperature field inside the drop undergoing bag breakup is very different. There is essentially no recirculation inside the drop and the coldest fluid is at the centerline of the drop. Since there is a large wake behind the drop, the cold thermal wake is much larger than for the low Eo drop. The drop undergoing shear breakup has only a small thermal wake, but the large deformation of the drop leads to a large heat transfer

rate.

In Figure 18, the evolution of the average temperature is presented for the three drops examined above. Initially the drops gain heat at approximately the same rate, but as they start to deform, the rate depends strongly on the breakup mode. The heat transfer rate is slowest for the nearly spherical drop and quickly increases as the Eo increases. As Figure 16 showed, the rate of increase of surface area increases greatly as Eo is increased. However, the flow field is also different and convective heat transfer changes. How much of the increased heat transfer can be attributed to increased surface area and how much to increased convection has not been examined in detail yet.

FIGURES

FIG. 1. Schematic diagram of the computational domain.

FIG. 2. Evolution of impulsively started drops with $Re = 242$, $Re_d = 1935$, and $\rho_d/\rho_o = 10$. Results for ten We are shown as denoted by the numbers below the figures. The numbers next to the drops denote t^* when the interfaces are plotted. The centroid of the drops in a column are separated by a fixed distance. The gap between two successive drops in a column does not represent the distance the drop travels during the time interval. The computations were done on a 256×512 grid.

FIG. 3. Non-dimensionalized aspect ratio, centroid velocity, and surface area plotted versus t^* for selected cases of the drops shown in Figure 2. Results for five $We = 3.74, 12.5, 18.7, 37.4$, and 93.5 are compared. $Re = 242$, $Re_d = 1935$, and $\rho_d/\rho_o = 10$.

FIG. 4. Vorticity contours (left) and streamlines (right) for the drop shown in Figure 2(d).

FIG. 5. Vorticity contours (left) and streamlines (right) for the drop shown in Figure 2(i).

FIG. 6. Inviscid flow simulations for $We = 93.5$ and $\rho_d/\rho_o = 10$ with three different values of $\delta = 0.0125$ (a); 0.01 (b); 0.0075 (c). In (d), the viscous result shown in Figure 2(i) is included for comparison. The drop shapes are plotted every $t^* = 0.4835$ in each column.

FIG. 7. Centroid velocities of the drops shown in Figure 6 plotted versus t^* .

FIG. 8. Evolution of impulsively started drops with $Re = 331$, $Re_d = 381$, and $\rho_d/\rho_o = 1.15$. Results for five We are shown as denoted by the numbers below the figures. The numbers inside the frames denote t^* when the interfaces are plotted. The computations were done on a 128×256 grid.

FIG. 9. Non-dimensionalized aspect ratio, centroid velocity, and surface area plotted versus t^* for the drops shown in Figure 8. Results for five $We = 2.73, 13.7, 27.4, 54.7$, and ∞ are compared. $Re = 331$, $Re_d = 1935$, and $\rho_d/\rho_o = 1.15$.

FIG. 10. Effects of the Reynolds number are shown for drops with $\rho_d/\rho_o = 10$ and $Re_d = 1935$. In the top row (a), $We = 18.7$ and evolutions of drops with four different Reynolds numbers, $Re = 387, 242, 121, 60.5$ (from left to right) are compared. In the bottom row (b), a similar comparison is made for $We = 74.8$ with the same set of the Reynolds numbers. The numbers next to the drops denote t^* when the interfaces are plotted. The centroid of the drops in a column are separated by a fixed distance. The gap between two successive drops in a column does not represent the distance the drop travels during the time interval. The computations were done on a 256×512 grid.

FIG. 11. Non-dimensional surface area plotted versus t^* are compared for four Reynolds numbers, $Re = 60.5, 121, 242$, and 387 . In (a), results for the $We = 18.7$ drops shown in Figure 10(a) are presented and in (b), those for the $We = 74.8$ drops in Figure 10(b) are shown.

FIG. 12. Drop viscosity effect on the deformation of drops with $\rho_d/\rho_o = 10$ and $Re = 242$. The number in each frame denotes the dimensionless time when the drop is plotted.

FIG. 13. Breakup mode maps for impulsively started drops with $Re_d = 1935$. The density ratios are 10 and 1.15 in (a) and (b), respectively.

FIG. 14. Eo effect on drop deformation: $\rho_d/\rho_o = 1.15$, $Oh_o = 0.05$, $Oh_d = 0.0466$. The drops are accelerated by a constant body force. The drop evolutions are shown for four Eo . The time intervals between successive interfaces, Δt_p^* are (a) 2.5; (b) 3.953; (c) 5.590; (d) 3.873. The grid are 256×1280 in (b) and (c) and 256×768 in (a) and (d). The dashed line in (a) and (d) represents the actual bottom boundary of the computational domain.

FIG. 15. Vorticity contours (left) and streamlines (right) for the drops shown in Figure 14 (b) and (d). The $Eo = 24$ drop is plotted at $t^* = 63.2$ and the $Eo = 144$ drop is plotted at $t^* = 11.6$.

FIG. 16. Non-dimensionalized surface area plotted versus t^* for the drops shown in Figure 14 (a)–(d).

FIG. 17. Simulations of the heat transfer during drop breakup for $Eo = 2.4, 24$, and 144 . Temperature field and drop contour are plotted for three drops shown in Figure 14 (a), (b), and (d) at selected times. $Oh = 0.05$, $Pr = 1$, $\rho_d/\rho_o = 1.15$, $\mu_d/\mu_o = 0.2$, $c_{pd}/c_{po} = 1$, and $k_d/k_o = 0.2$

FIG. 18. Average temperature plotted versus time for the drops shown in Figure 17.

Figure 1

19

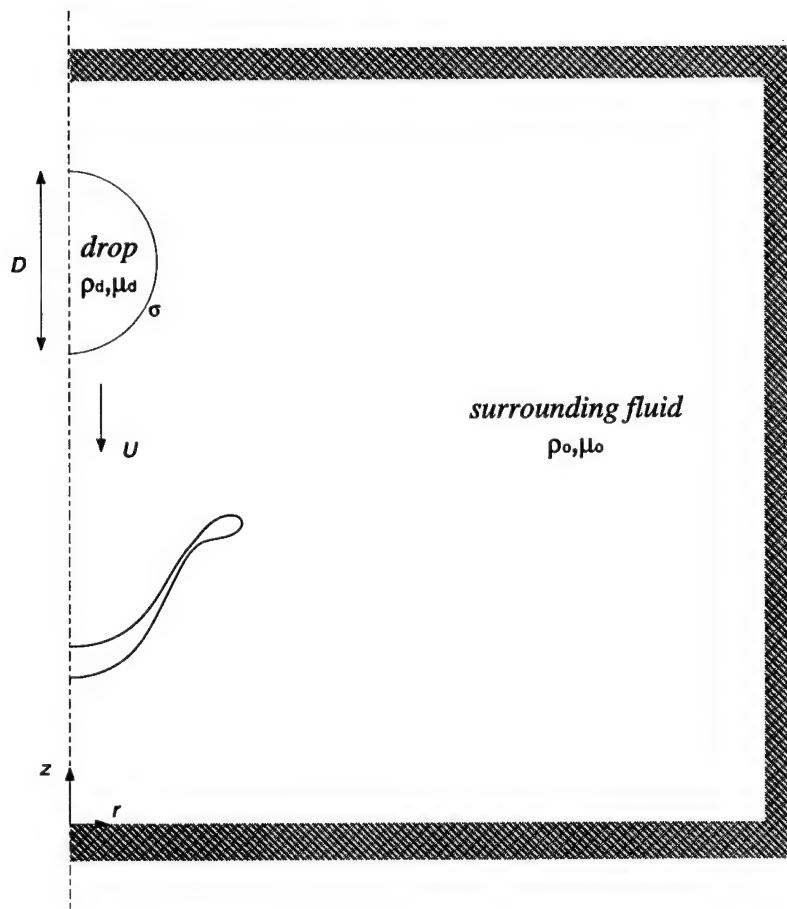


Figure 2

20

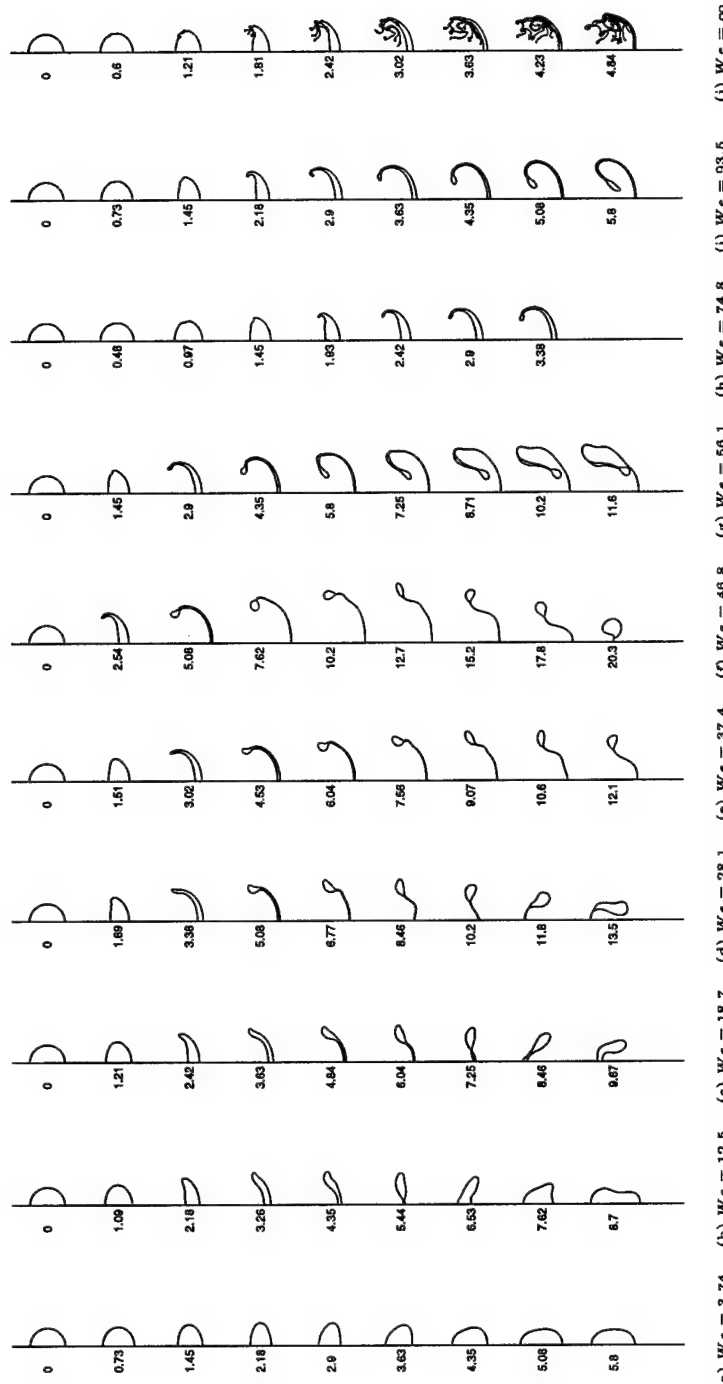
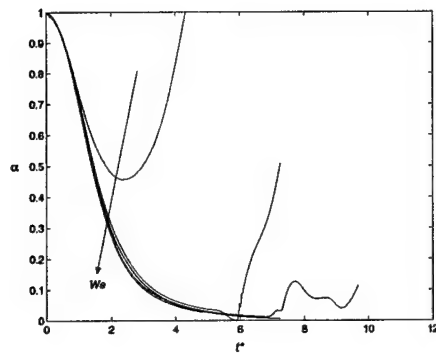
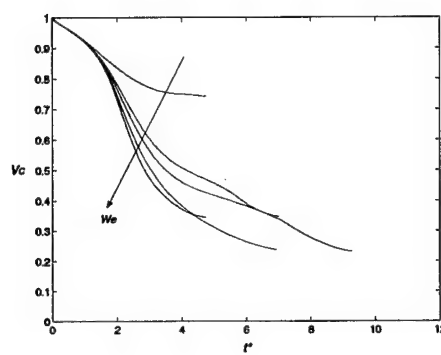
(a) $W\epsilon = 3.74$ (b) $W\epsilon = 12.5$ (c) $W\epsilon = 18.7$ (d) $W\epsilon = 28.1$ (e) $W\epsilon = 37.4$ (f) $W\epsilon = 46.8$ (g) $W\epsilon = 56.1$ (h) $W\epsilon = 74.8$ (i) $W\epsilon = 93.5$ (j) $W\epsilon = \infty$

Figure 3

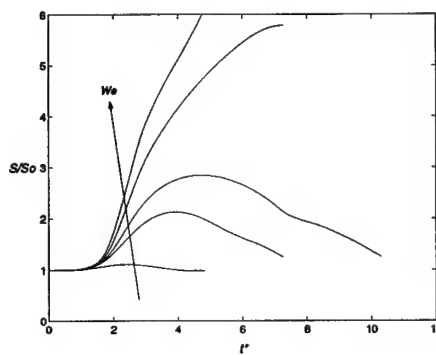
21



(a) aspect ratio



(b) centroid velocity



(c) surface area

Figure 4

22

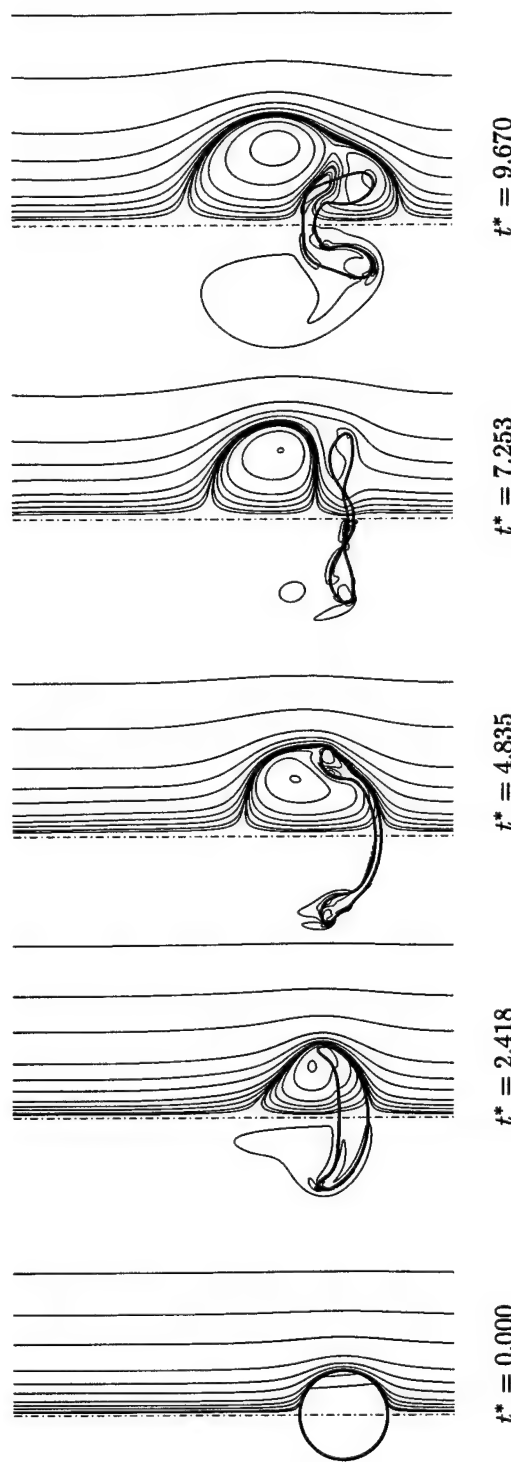
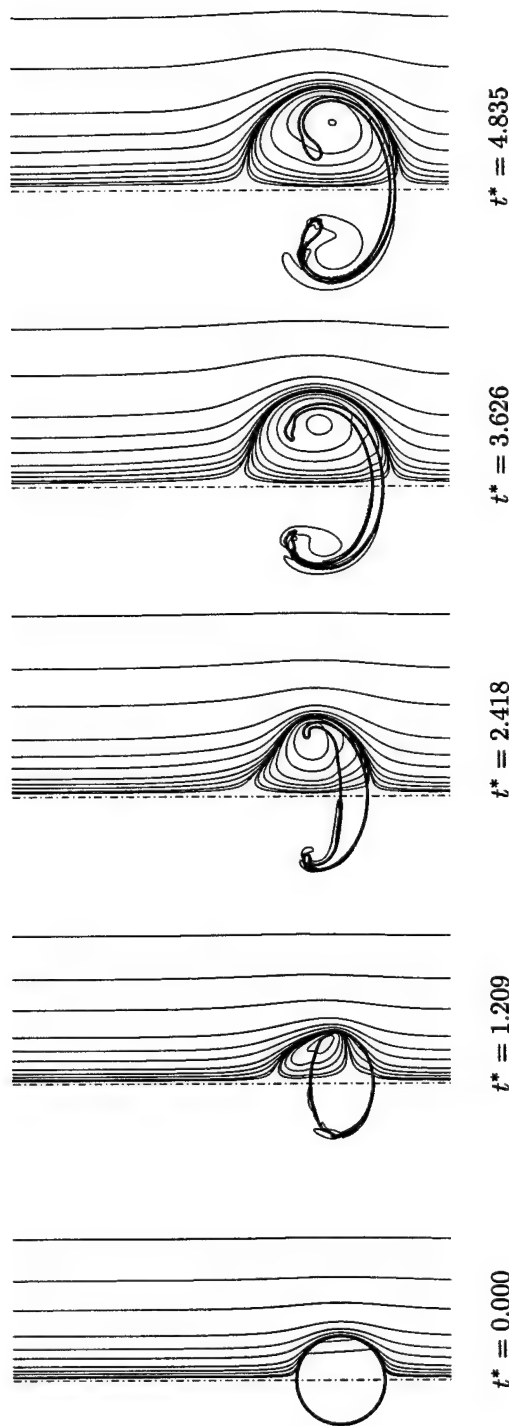


Figure 5

23



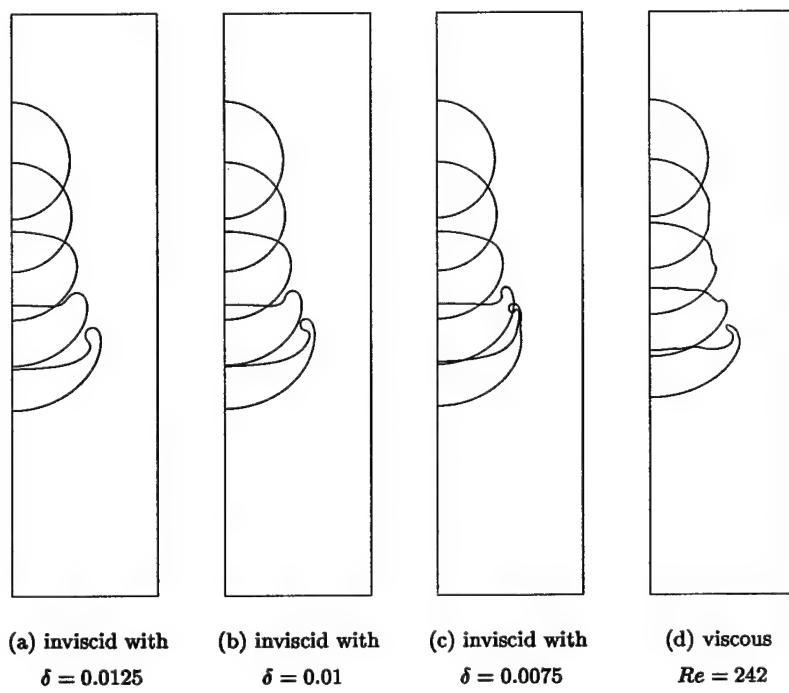


Figure 7

25

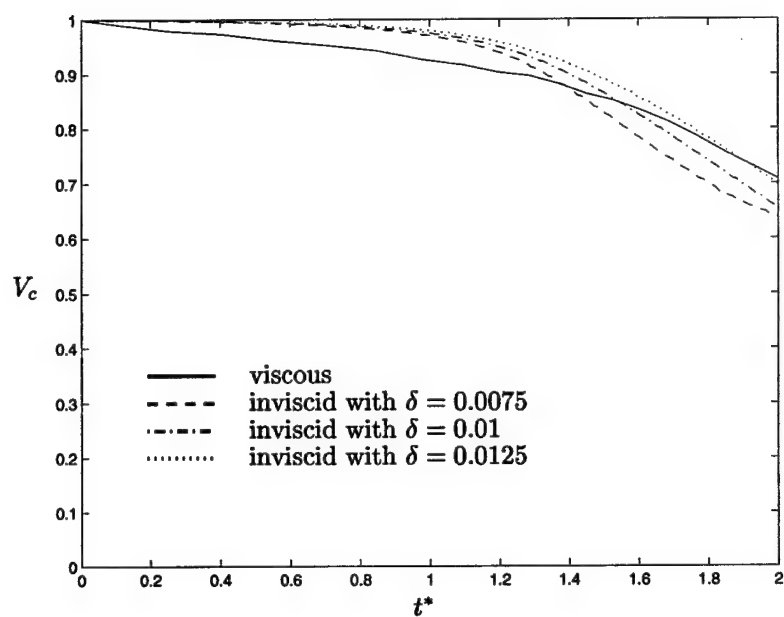


Figure 8

26

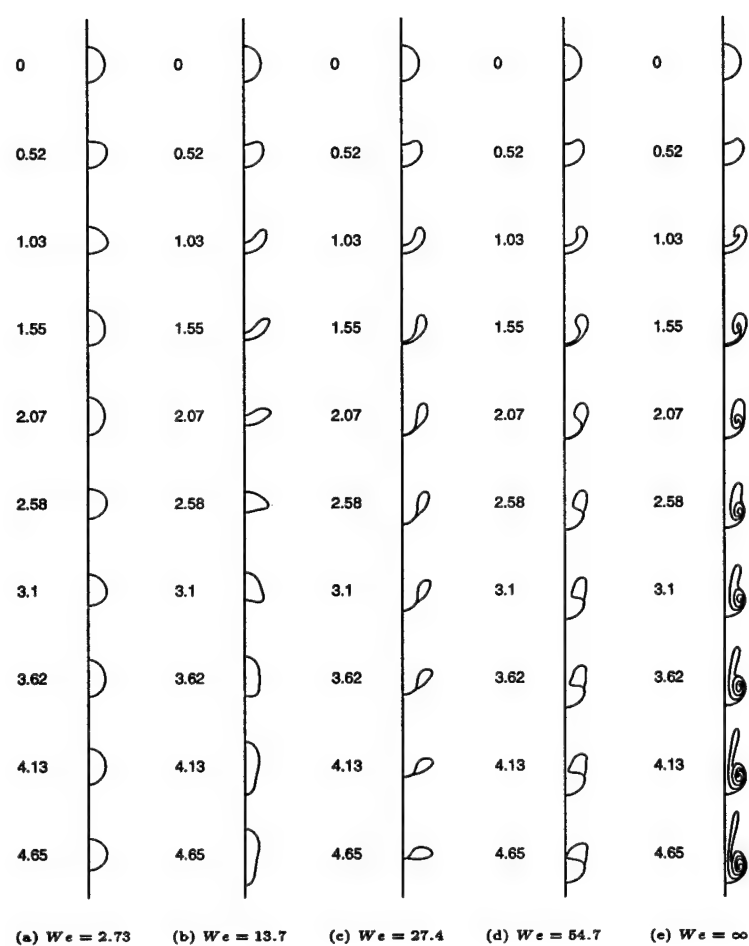
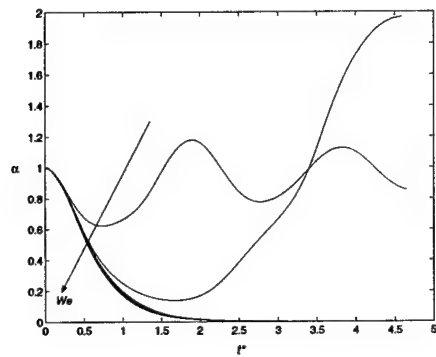
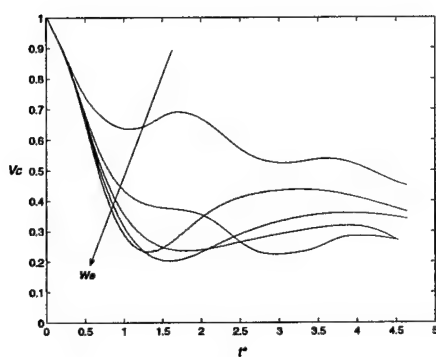


Figure 9

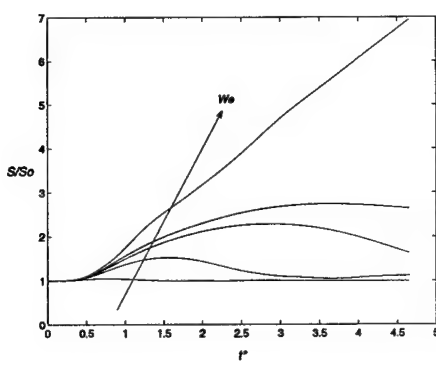
27



(a) aspect ratio



(b) centroid velocity



(c) surface area

Figure 10

28

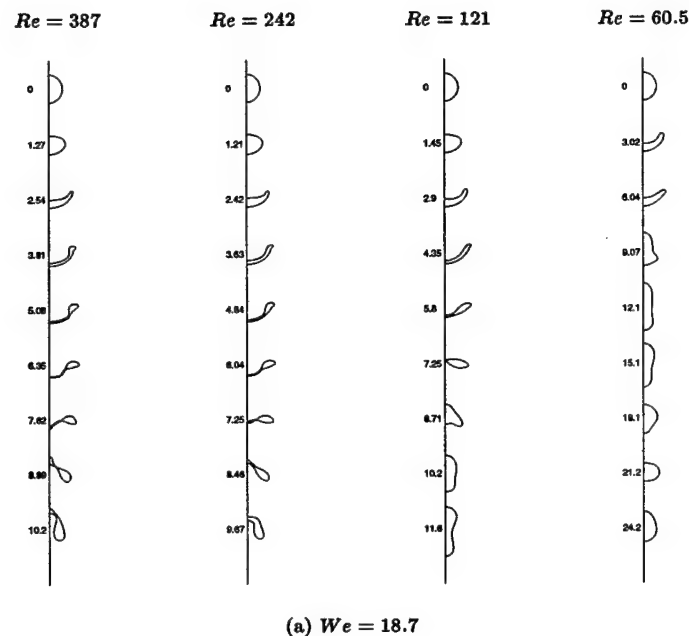
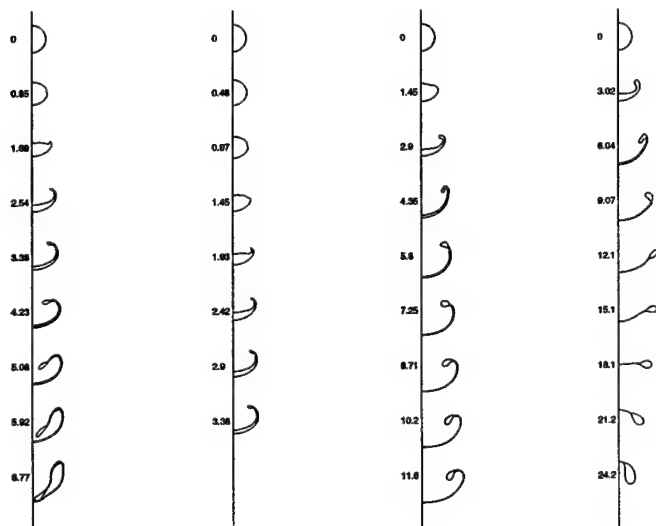
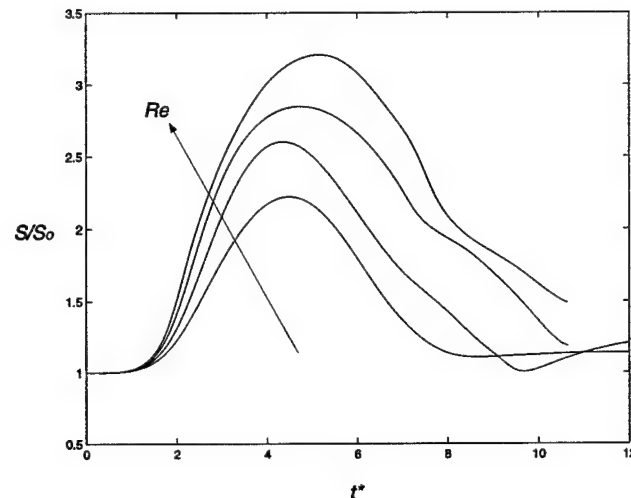
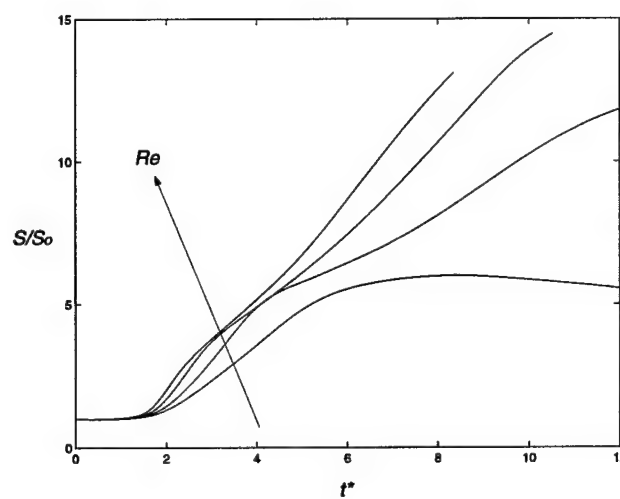
(a) $We = 18.7$ (b) $We = 74.8$

Figure 11

29



(a) $We = 18.7$



(b) $We = 74.8$

Figure 12

30

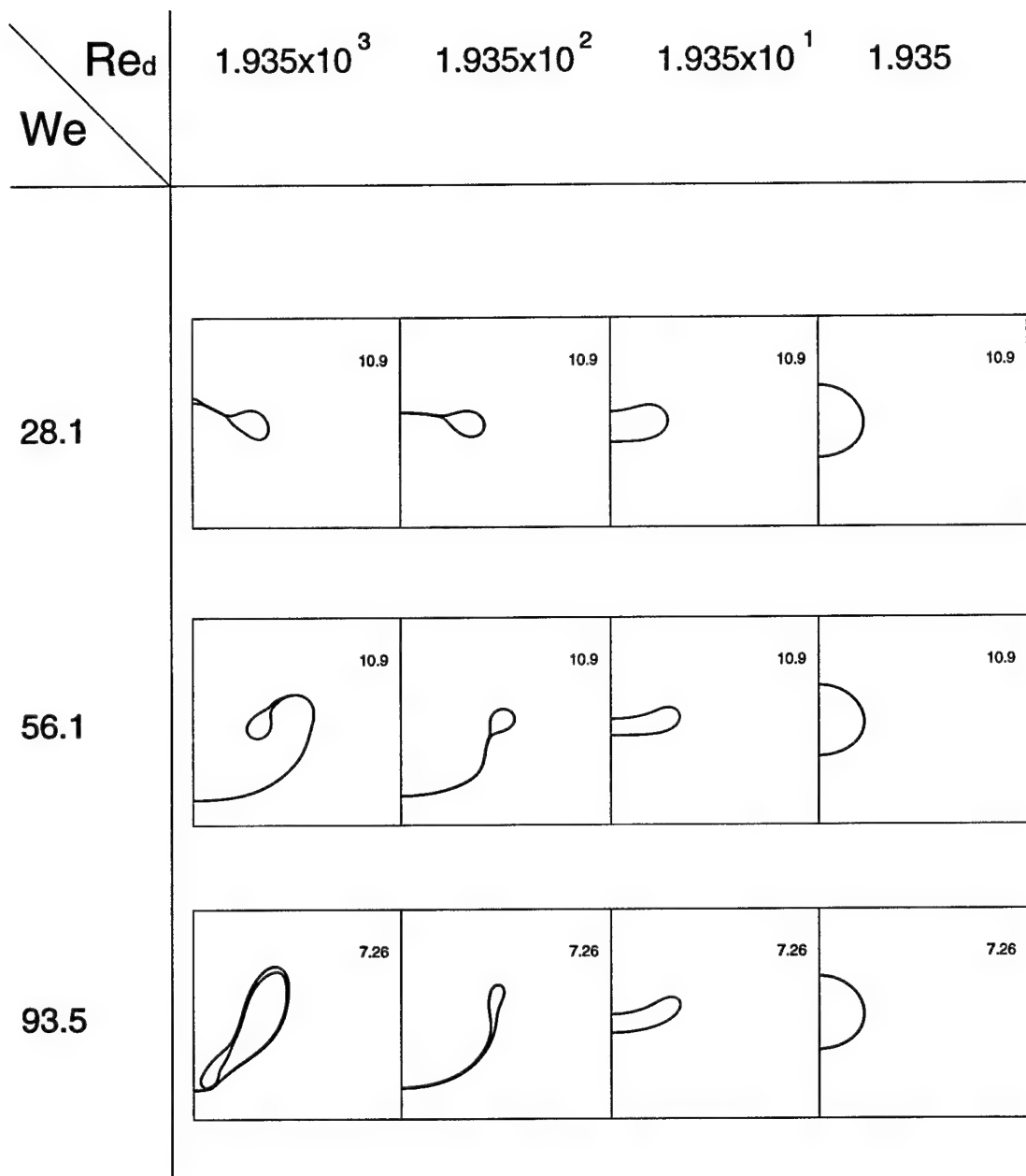


Figure 13

31

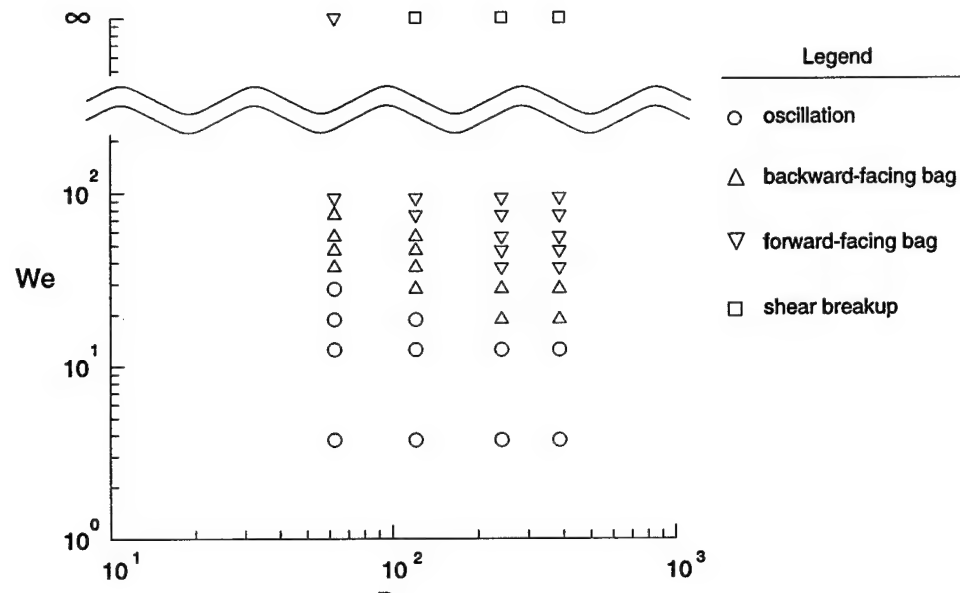
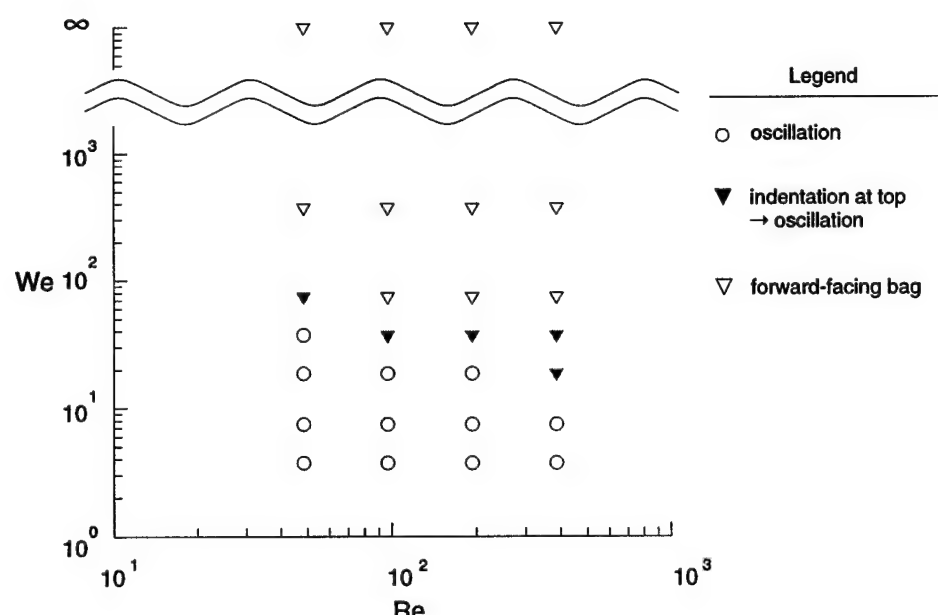
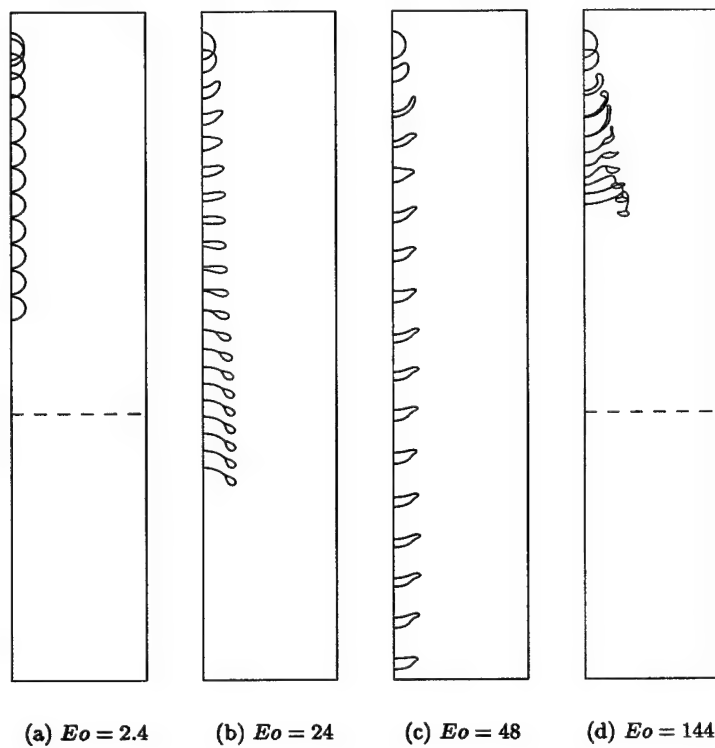
(a) $\rho_d/\rho_o = 10$ (b) $\rho_d/\rho_o = 1.15$

Figure 14

32



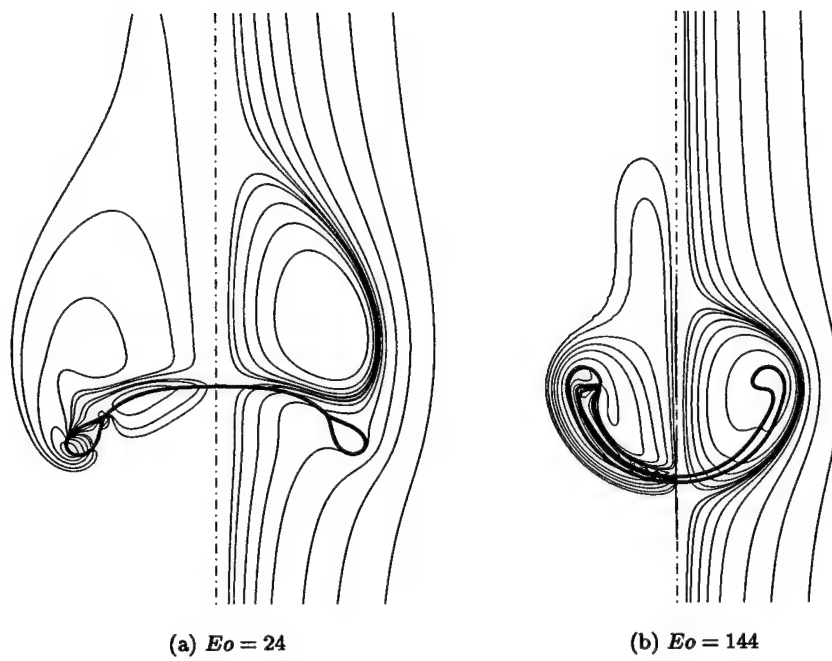


Figure 16

34

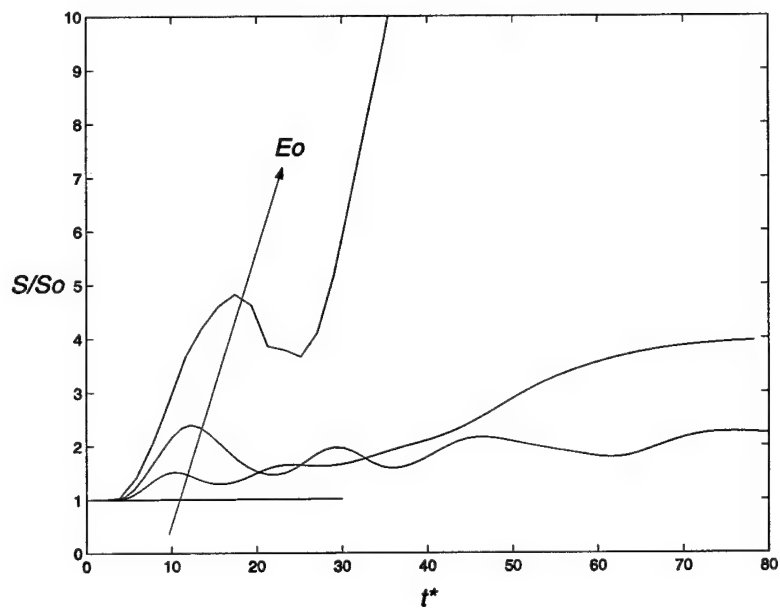
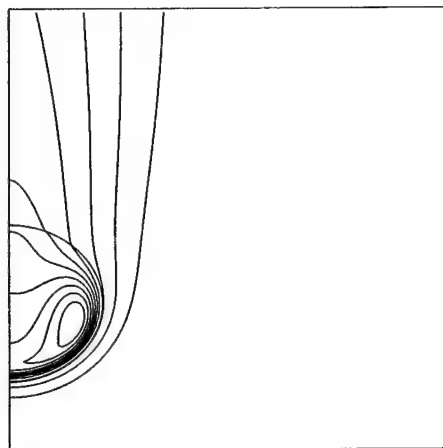
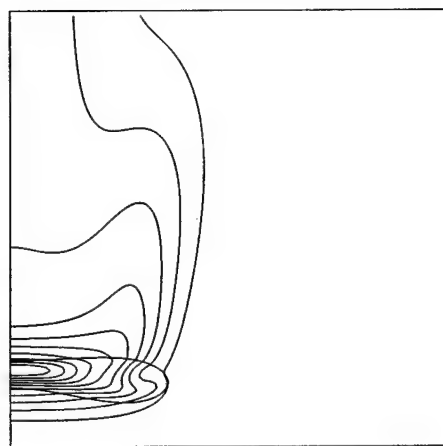


Figure 17

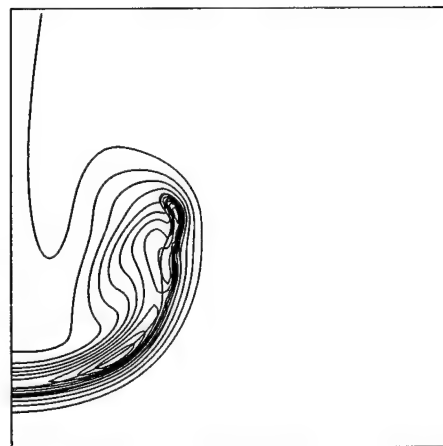
35



(a) $Eo = 2.4$



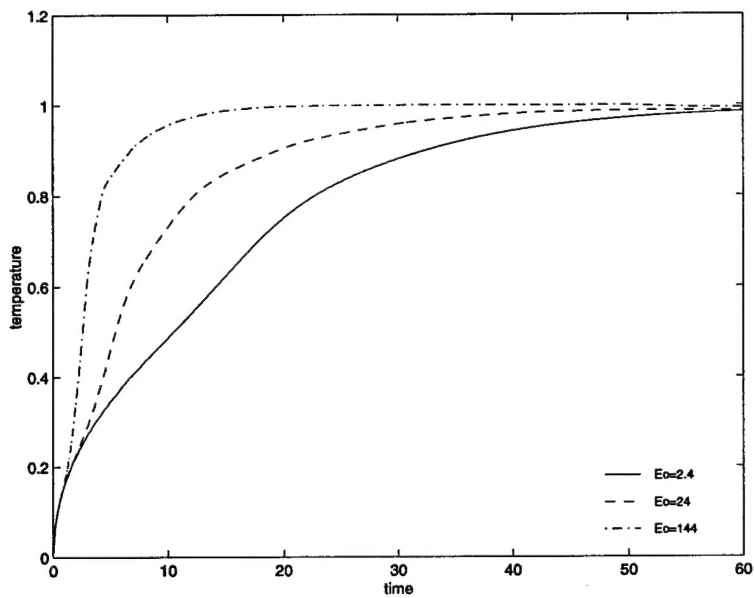
(b) $Eo = 24$



(c) $Eo = 144$

Figure 18

36



REFERENCES

- ¹ W. R. Lane, "Shatter of Drops in Streams of Air," *Industrial and Engineering Chemistry* **43**, 1312 (1951).
- ² J. O. Hinze, "Fundamentals of the Hydrodynamic Mechanism of Splitting in Dispersion Process," *A.I.Ch.E. Journal* **1**, 289 (1955).
- ³ A. R. Hanson, E. G. Domich, and H. S. Adams, "Shock Tube Investigation of the Breakup of Drops by Air Blasts," *Phys. Fluids* **6**, 1070 (1964).
- ⁴ A. A. Ranger and J. A. Nicholls, "Aerodynamic Shattering of Liquid Drops," *AIAA Journal* **7**, 285 (1969).
- ⁵ B. E. Gel'fand, S. A. Gubin, S. M. Kogarko, and S. P. Komar, "Singularities of the Breakup of Viscous Liquid Droplets in Shock Waves," *J. Eng. Phys.* **25**, 1140 (1973).
- ⁶ S. A. Krzczkowski, "Measurement of Liquid Droplet Disintegration Mechanisms," *Int. J. Multiphase Flow* **6**, 227 (1980).
- ⁷ A. A. Borisov, B. E. Gel'fand, M. S. Natanzon, and O. M. Kossov, "Droplet Breakup Regimes and Criteria for Their Existence," *J. Eng. Phys.* **40**, 44 (1981).
- ⁸ R. D. Reitz, and F. V. Bracco, "Mechanism of Breakup of Round Liquid Jets," *Encyclopedia of Fluid Mechanics* (Gulf Pub., Houston, TX, 1986), Vol. 3.
- ⁹ M. Pilch and C. A. Erdman, "Use of Breakup Time Data and Velocity History Data to Predict the Maximum Size of Stable Fragments for Acceleration-Induced Breakup of a Liquid Drop," *Int. J. Multiphase Flow* **13**, 741 (1987).
- ¹⁰ A. Wierzba, "Deformation and Breakup of Liquid Drops in a Gas Stream at Nearly Critical Weber Numbers," *Experiments in Fluids* **9**, 59 (1990).
- ¹¹ L.-P. Hsiang and G. M. Faeth, "Near-Limit Drop Deformation and Secondary Breakup," *Int. J. Multiphase Flow* **18**, 635 (1992).

- ¹² L.-P. Hsiang and G. M. Faeth, "Drop Properties after Secondary Breakup," *Int. J. Multiphase Flow* **19**, 721 (1993).
- ¹³ L.-P. Hsiang and G. M. Faeth, "Drop Deformation and Breakup due to Shock Wave and Steady Disturbances," *Int. J. Multiphase Flow* **21**, 545 (1995).
- ¹⁴ D. D. Joseph, J. Belanger, and G. S. Beavers, "Breakup of a Liquid Drop Suddenly Exposed to a High-Speed Airstream," *Int. J. Multiphase Flow* **25**, 1263 (1999).
- ¹⁵ R. I. Nigmatulin, *Dynamics of Multiphase Media 1* (Hemisphere Publishing Corporation, 1991).
- ¹⁶ J. B. Heywood, *Internal Combustion Engine Fundamentals* (McGraw-Hill, 1988), p. 522.
- ¹⁷ S. O. Unverdi and G. Tryggvason, "A Front-Tracking Method for Viscous, Incompressible, Multi-Fluid Flows," *J. Comput. Phys.* **100**, 25 (1992).
- ¹⁸ G. Tryggvason, B. Bunner, O. Ebrat, and W. Tauber, "Computations of Multiphase Flows by a Finite Difference/Front Tracking Method – I. Multi-Fluid Flows," 29th. Computational Fluid Dynamics, von Karman Institute for Fluid Dynamics Lecture Series 1998-03 (1998).
- ¹⁹ M. Abramowitz, *Handbook of Mathematical Functions, with Formulas, Graphs, and Mathematical Tables* (Dover, New York, 1973).
- ²⁰ S. S. Sadhal, P. S. Ayyaswamy, and J. N. Chung, *Transport Phenomena with Drops and Bubbles* (Springer-Verlag, New York, 1996).
- ²¹ C. H. Lee and R. D. Reitz, "An Experimental Study of the Effect of Gas Density on the Distortion and Breakup Mechanism of Drops in High Speed Gas Stream," *Int. J. Multiphase Flow* **26**, 229 (2000).
- ²² Abramzon, B. and Borde, I., "Conjugate Unsteady Heat Transfer from a Droplet in Creeping Flow," *AIChE J.*, **26**, 536 (1980).
- ²³ Chiang, C. H., Raju, M. S., and Sirignano, W. A., "Numerical Analysis of Convecting, Vaporizing Fuel Droplet with Variable Properties," *Int. J. Heat Mass Transfer*, **35**, 1307 (1992).

²⁴ Chiang, C. H. and Sirignano, W. A., "Interacting, Convecting, Vaporizing Fuel Droplets with Variable Properties," *Int. J. Heat Mass Transfer*, **36**, 875 (1993).

²⁵ Haywood, R. J., Renksizbulut, M., and Raithby, G. D., "Numerical Solutions of Deforming Evaporating Droplets at Intermediate Reynolds Numbers," *Numer. Heat Transfer, Part A*, **26**, 253 (1994).